Supplementary information

Suppressing Dendrites via Lateral Lithium Flux in Li Metal Solid-State Batteries

Authors: Huanyu Zhang[a,b]†, Faruk Okur[a,b]†, Matthias Klimpel[a,b], Julian F. Baumgärtner[a,b], Jaka Šivavec[a,b], André Müller[b], Ihor Neporozhnii[c], Orhan Kibrisli[c], Oleksandr Voznyy[c], Yaroslav E. Romanyuk[b], Maksym V. Kovalenko[a,b]*, Kostiantyn V. Kravchyk[a,b]*

Affiliations:

[a] Laboratory of Inorganic Chemistry, Department of Chemistry and Applied Biosciences, ETH Zürich, 8093 Zürich, Switzerland

[b] Laboratory for Thin Films and Photovoltaics, Empa - Swiss Federal Laboratories for Materials Science & Technology, 8600 Dübendorf, Switzerland

[c] Department of Electrical and Computer Engineering, University of Toronto, 35 St. George Street, Toronto, Ontario M5S 1A4, Canada.

*Corresponding authors. Emails: mvkovalenko@ethz.ch and kostiantyn.kravchyk@empa.ch

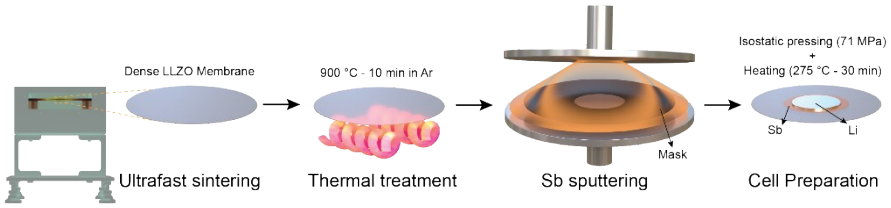

Fig. S1 Scheme of LLZO-Sb fabrication production.

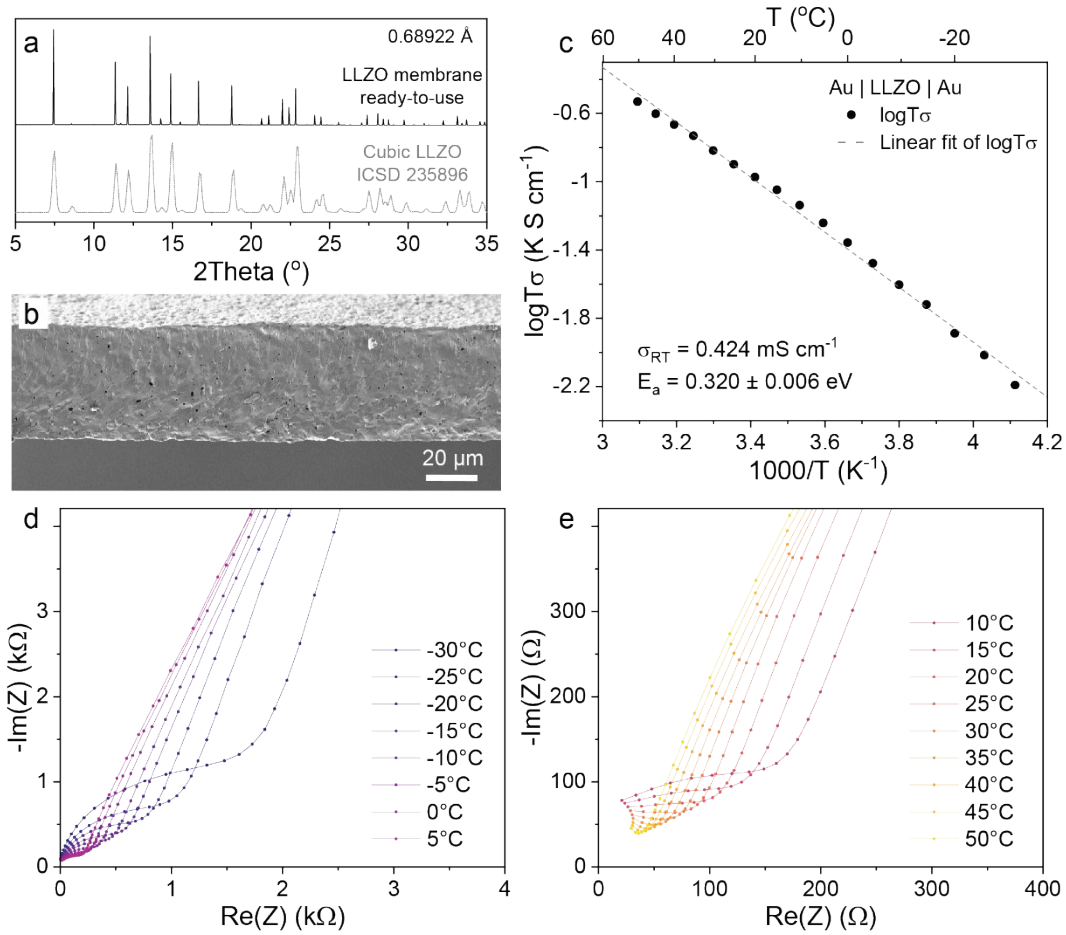

Fig. S2 Material characterization of bulk properties of LLZO membranes. (a) XRD pattern, (b) SEM image of LLZO membranes ready-to-use. (c) Arrhenius plot and (d-e) Nyquist diagram of Au | LLZO | Au symmetrical cells at temperature range from -30 °C to 50 °C.

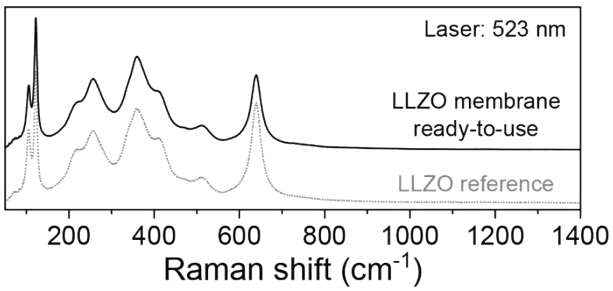

Fig. S3 Raman spectra of LLZO membranes ready-to-use.

Note S1 Characterization of LLZO membrane.

XRD and SEM measurements of the LLZO membranes (**Fig. S2 a-b**) confirmed that developed membranes are characterized by a high density and exhibited a phase-pure cubic LLZO structure (space group $Ia\bar{3}d$, with lattice parameters a = 12.9622(2) Å and volume V = 2177.89 $Å^3$, ICSD 235 896). The LLZO membranes were characterized by EIS using an Au | LLZO | Au symmetrical cell configuration (**Fig. S2 c-e**). The estimated Li-ion conductivity of the fabricated membranes was 0.424 mS cm^{-1} at RT. The activation energy was determined to be *ca.* 0.32 eV. The Raman measurements (**Fig. S3**) of the LLZO membranes showed pure cubic LLZO without surface contamination.

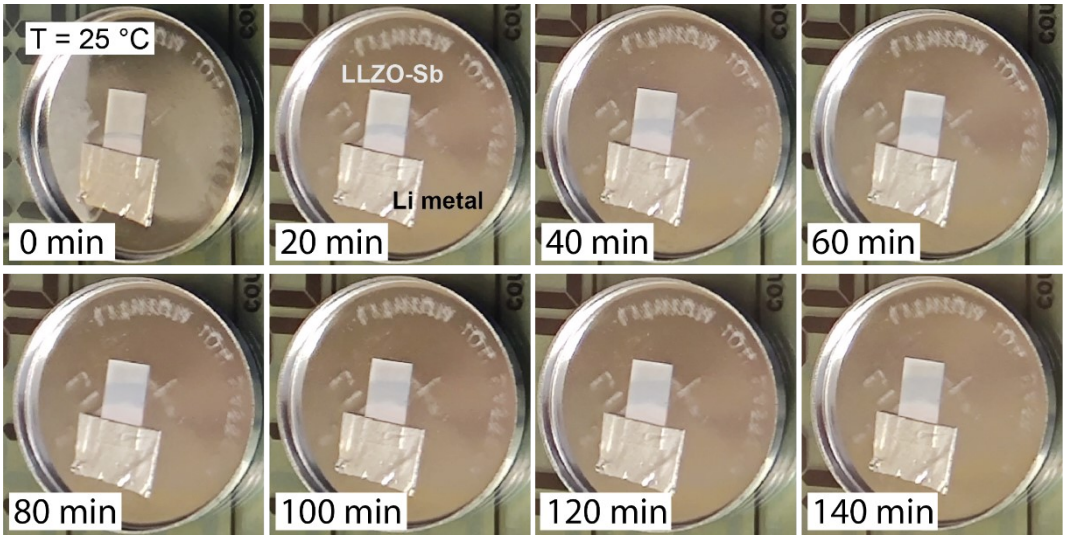

Fig. S4 Photos of Li-Sb alloying over time on 10 nm Sb sputtered LLZO membrane at 25 °C.

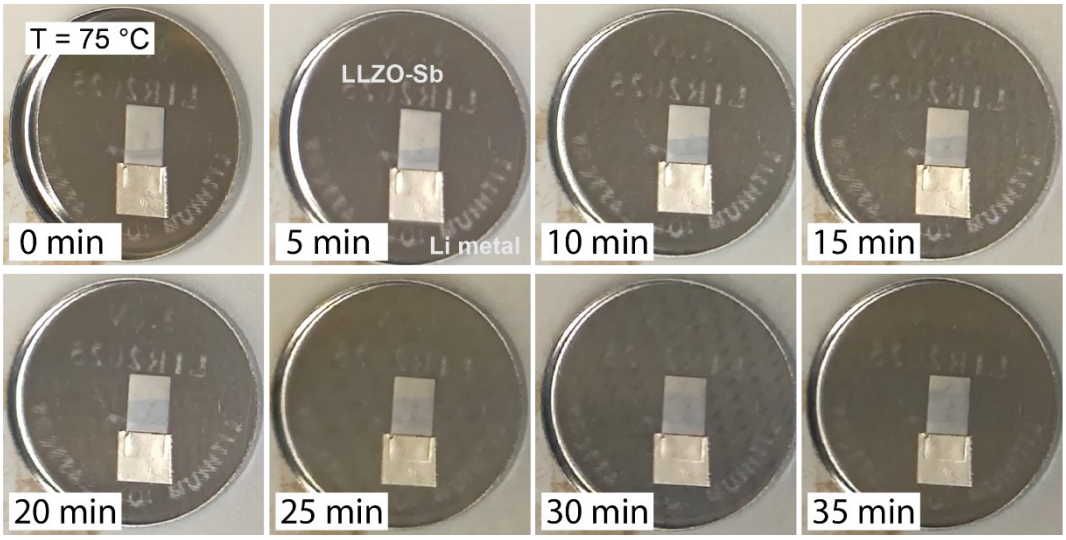

Fig. S5 Photos of Li-Sb alloying over time on 10 nm Sb sputtered LLZO membrane at 75 ºC.

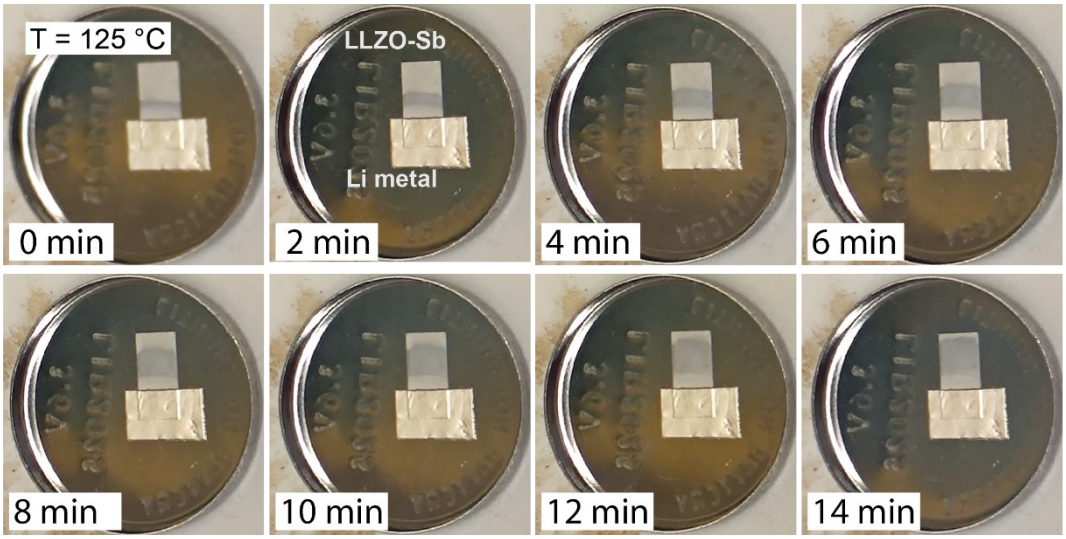

Fig. S6 Photos of Li-Sb alloying over time on 10 nm Sb sputtered LLZO membrane at 125 ºC.

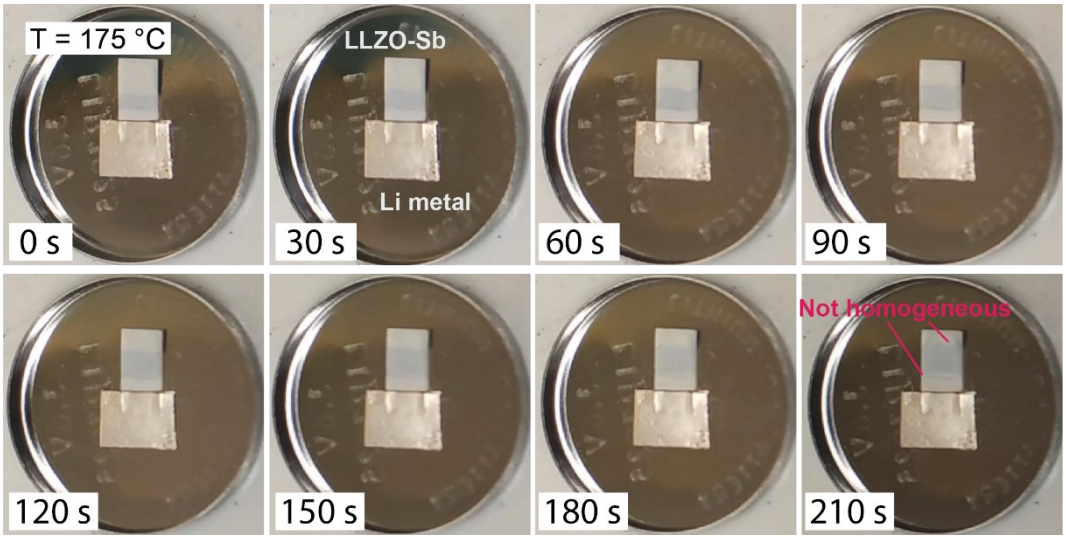

Fig. S7 Photos of Li-Sb alloying over time on 10 nm Sb sputtered LLZO membrane at 175 °C.

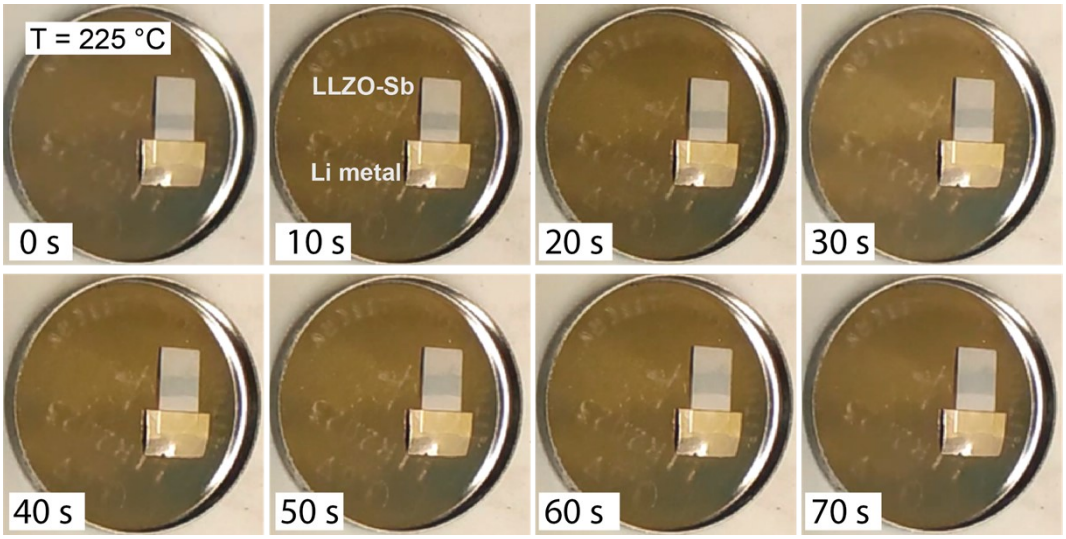

Fig. S8 Photos of Li-Sb alloying over time on 10 nm Sb sputtered LLZO membrane at 225 °C.

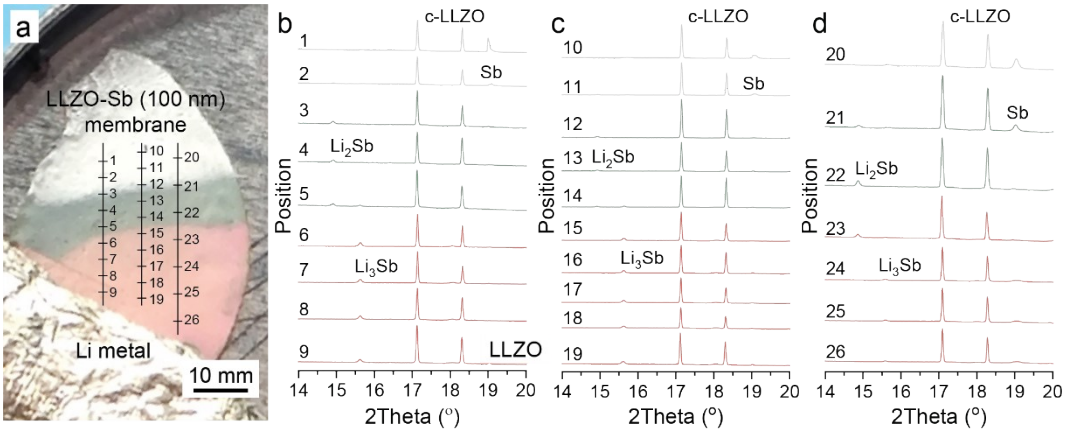

Fig. S9 Identification of Sb, Li_2Sb, and Li_3Sb on LLZO surface. (a) SGIXRD mapping and (b-d) patterns of LLZO membrane with different regions of Li-Sb alloy.

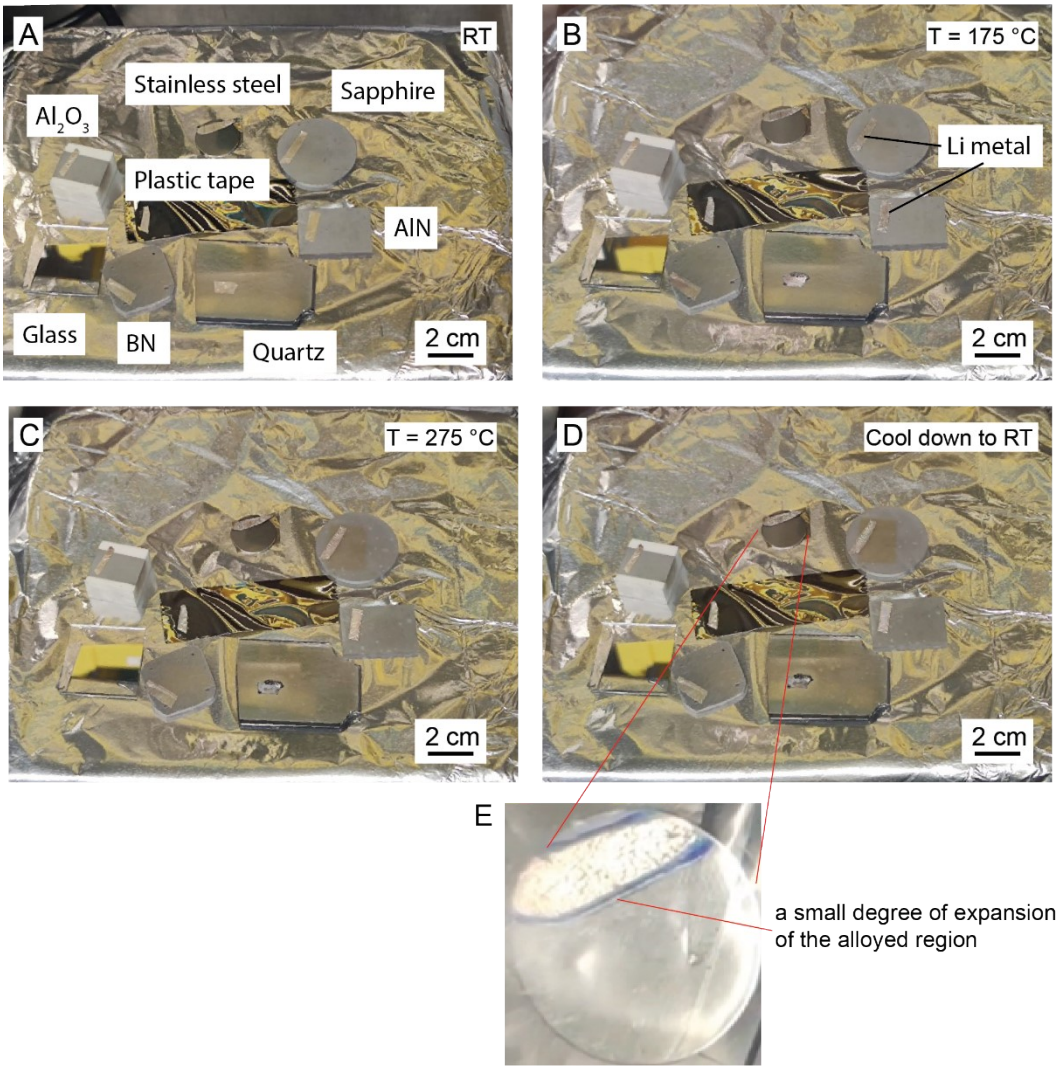

Fig. S10 Photos of Li-Sb alloy formation experiments on different substrates. After 10 nm of Sb was sputtered, a small piece of Li was pressed on each of these substrates. The spreading of Li-Sb alloy was not observed after heating up to 275 °C. The lateral propagation is strongly suppressed and confined to short distances, indicating that Li diffusion within the Li–Sb interlayer is present but limited in spatial extent. Such short-range diffusion is insufficient to sustain long-range lateral propagation over micrometer-scale distances. In contrast, the pronounced propagation observed on Li-ion-conducting LLZO substrates demonstrates that extended lateral transport requires Li^+ conduction through the solid-state electrolyte.

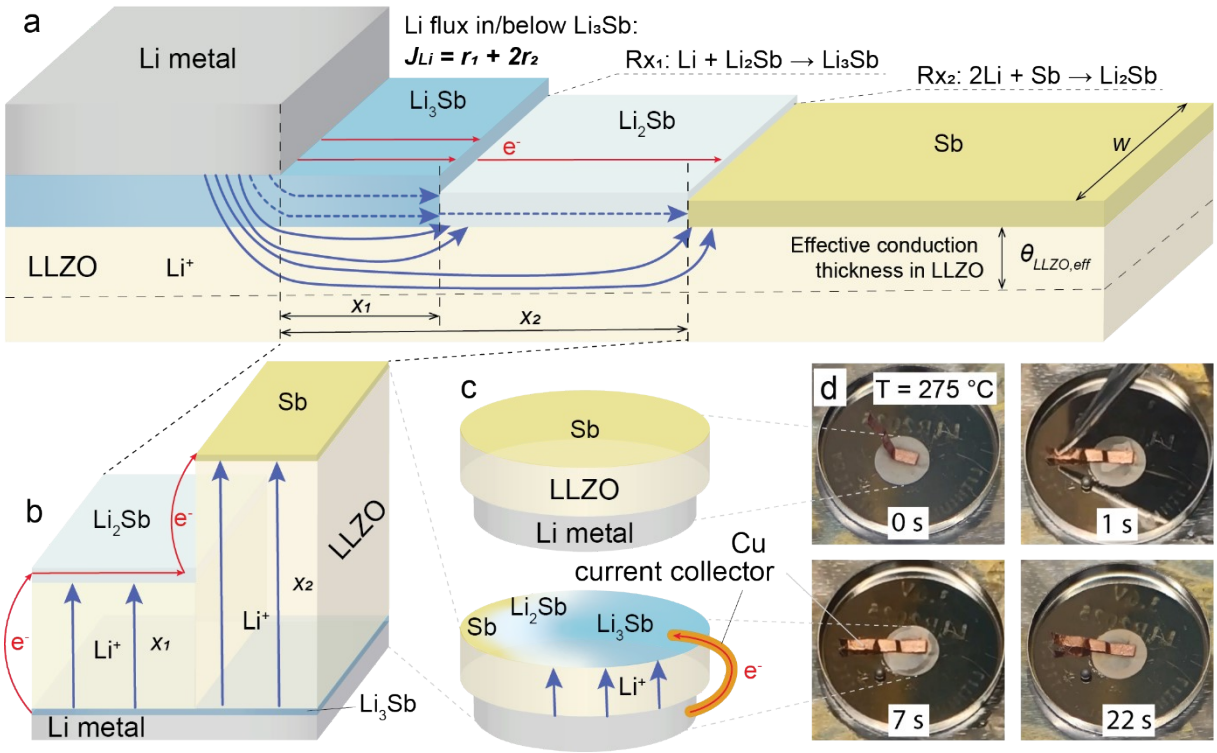

Fig. S11 Mechanism of lateral lithium flux at the Li | Li_3Sb IL | SSE interface. (a) Scheme of Li-Sb alloy formation process on LLZO surface (b) Equivalent self-discharge batteries of Li_2Sb | LLZO-Li_3Sb | Li and Sb | LLZO-Li_3Sb | Li. (c) Schemes and (d) photos of a self-discharge Sb | LLZO | Li battery at 275 °C.

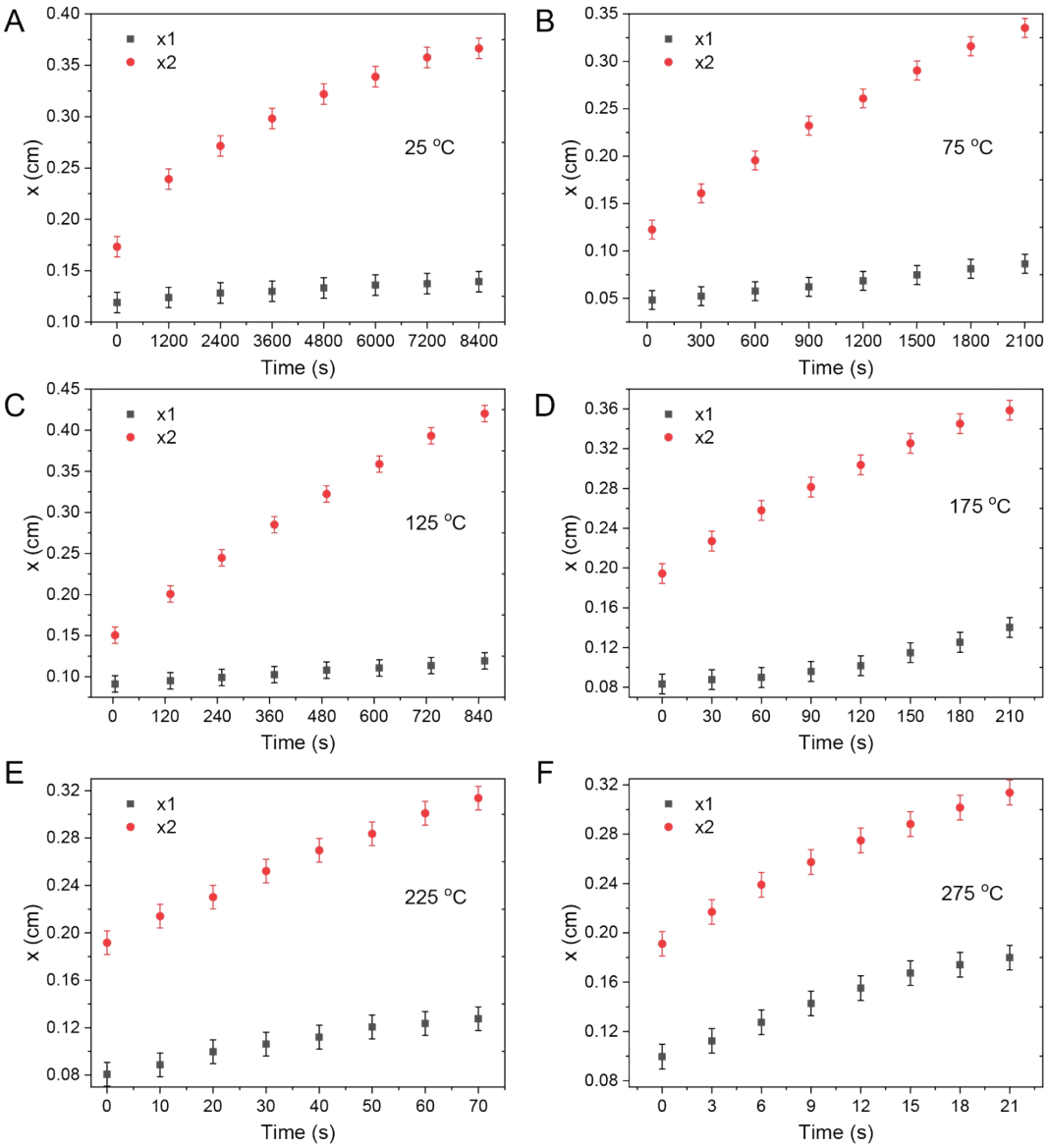

Fig. S12 Plots of recorded Li-Sb alloy crawling distances x_1 (Li_3Sb regions) and x_2 (Li_2Sb regions) versus time at different temperatures. Error bars represent uncertainty from spatial (±0.01 cm) and temporal (±0.1 s) resolution.

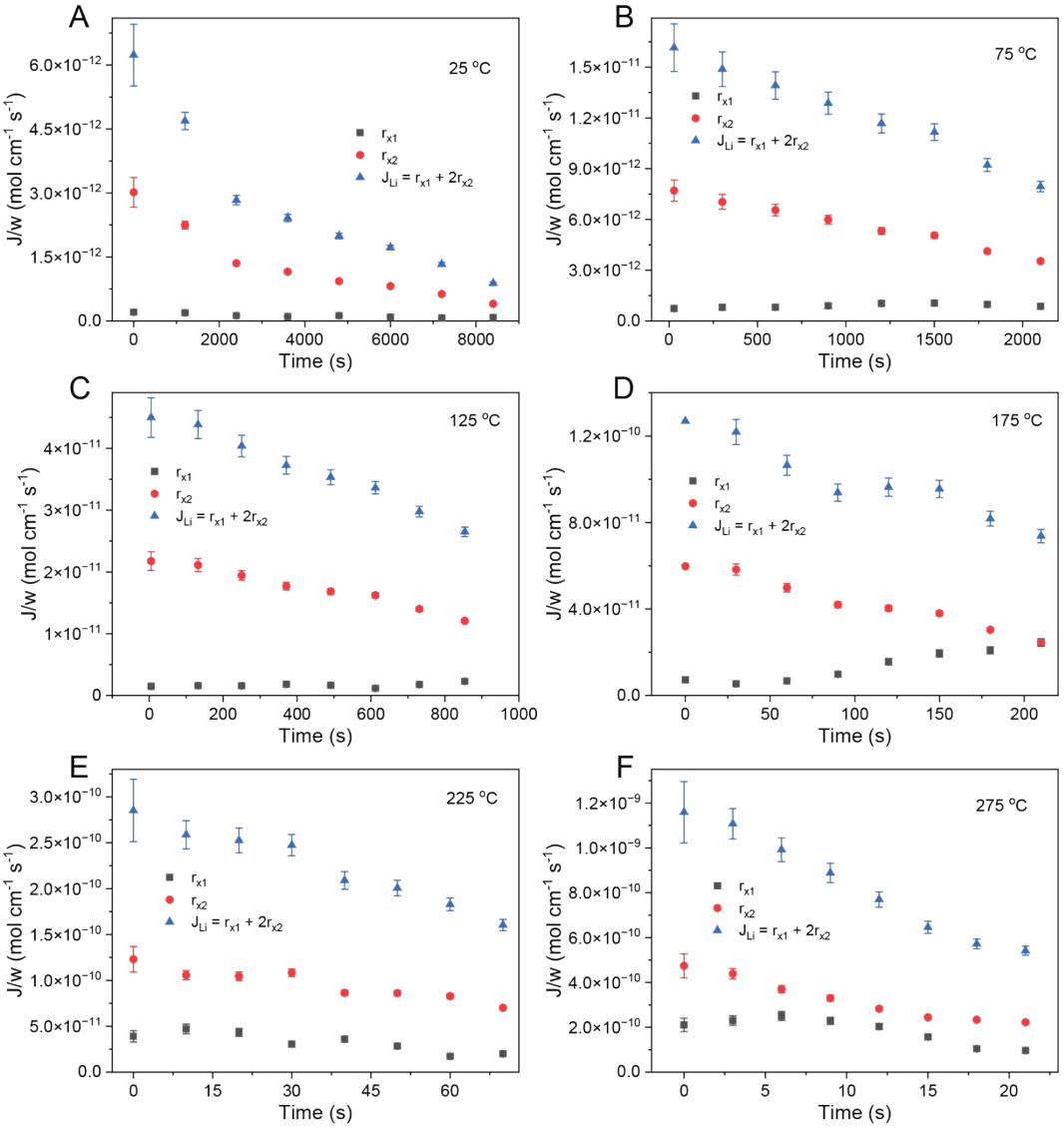

Fig. S13 Plots of specific areal rates $r_{1,A}$ (rate of Li_3Sb formation), $r_{2,A}$ (rate of Li_2Sb formation), and $J_{Li,A}$ (Li diffusion in Li_3Sb region) versus time at different temperatures.

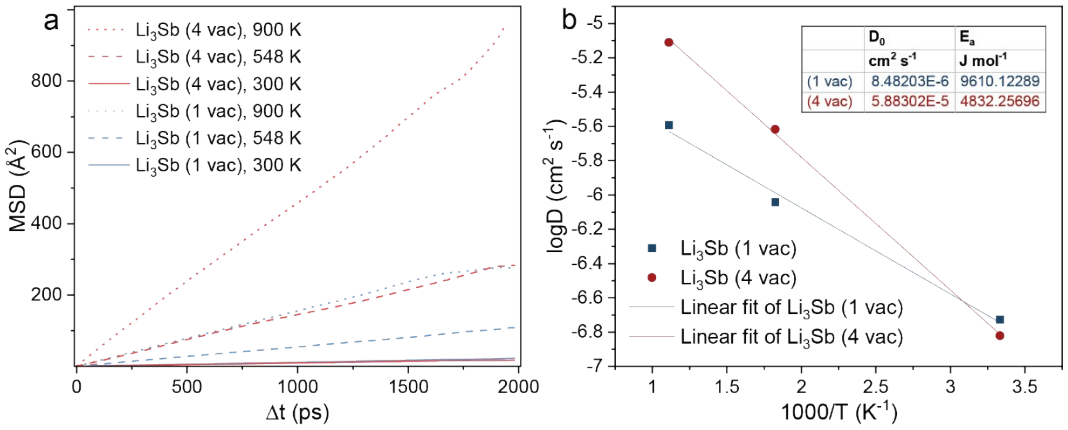

Fig. S14 Evaluation of Li diffusion in Li_3Sb IL. (a) Plot of MSD as a function of the diffusion time for Li_3Sb system with one and four vacancies at 300 K, 548 K, and 900 K. The diffusion process was simulated with ab initio molecular dynamics calculations using VASP DFT code. (b) Arrhenius plot of conductivity vs reciprocal temperature for Li_3Sb system with one and four vacancies obtained from ab initio molecular dynamics calculations using VASP DFT code.

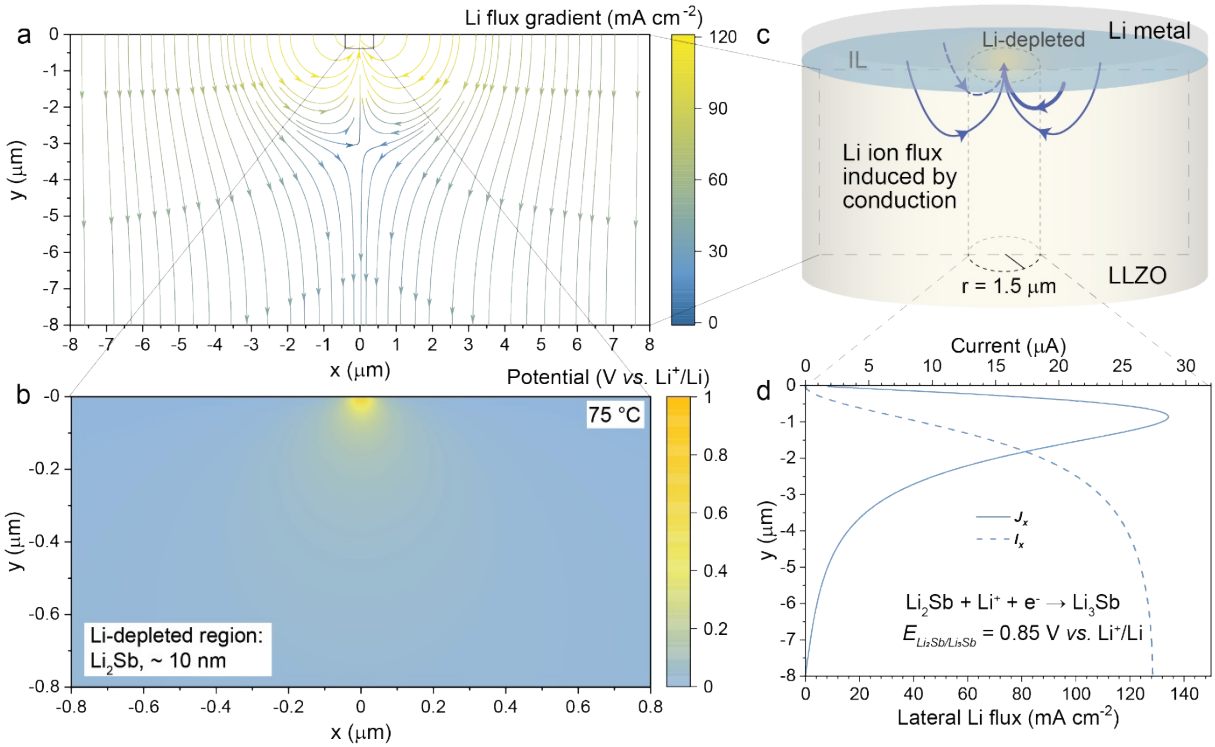

Fig. S15 Evaluation of lateral Li flux. (a) 2D Li flux distribution maps in LLZO are simulated assuming a Li-depleted region of Li_2Sb with a shape of 10 nm radius sphere at the Li_3Sb | LLZO interface, and (b) its corresponding potential maps, based on the model in scheme (c). (d) The lateral Li flux and current induced by the Li-depleted region as a function of effective conduction thickness in LLZO.

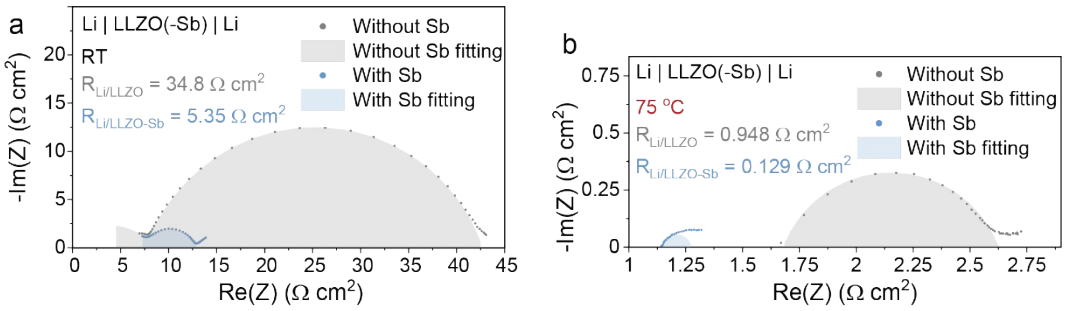

Fig. S16 Interfacial resistance of Li | LLZO interface with and without the Li_3Sb IL. Nyquist diagram of the LLZO membrane with/without 10 nm Sb coating measured at (a) room temperature and (b) 75 °C though the Li | LLZO | Li symmetrical cell configuration.

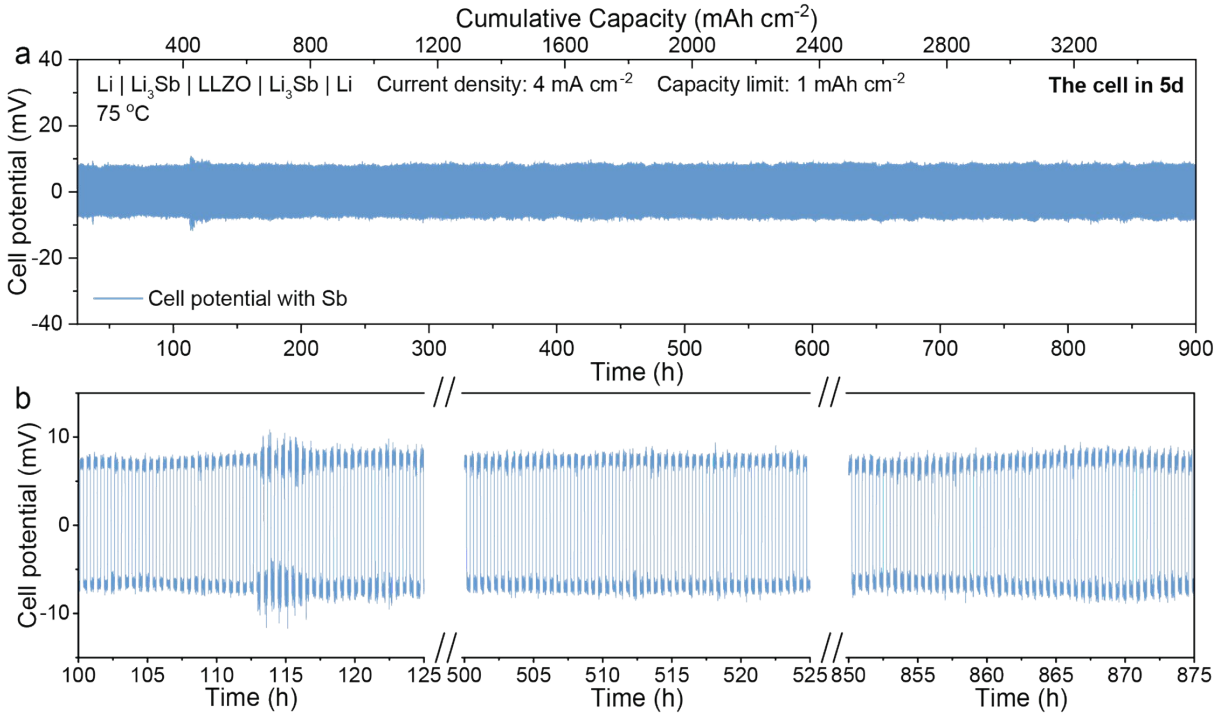

Fig. S17 Cyclic stability of Li | LLZO | Li symmetric cells with the Li_3Sb IL. Cell potential profile (a) and selected region (b) of galvanostatic cycling of Li | LLZO-Sb | Li symmetric cells prepared with LLZO membrane with Sb layer using 4 mA cm^{-2} current rate and 1 mAh cm^{-2} capacity limitation per each half cycle. Continuation of the cell in **Fig. 5d**.

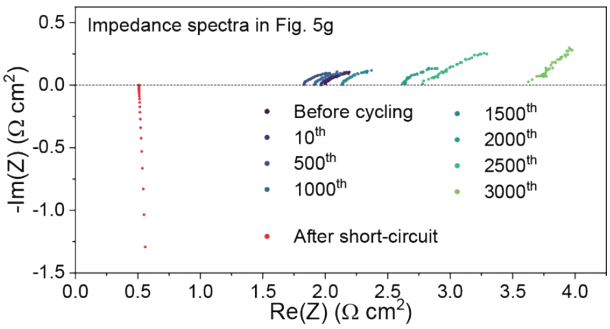

Fig. S18 Nyquist diagram of Li | Li_3Sb | LLZO | Li_3Sb | Li symmetrical cell in Fig. 5g.

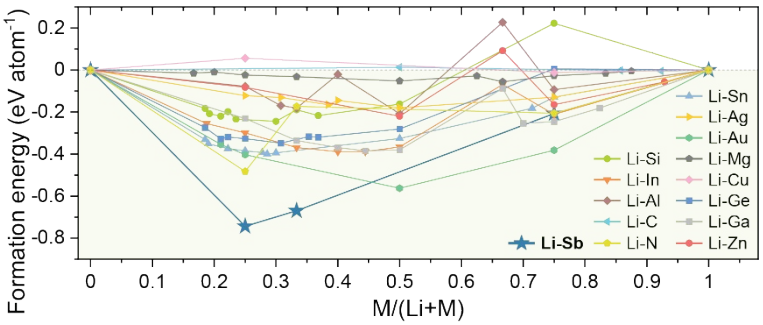

Fig. S19 Formation energy of possible Li-binary systems as a candidate for the IL. Data collected from *Materials Project*.[1, 2]

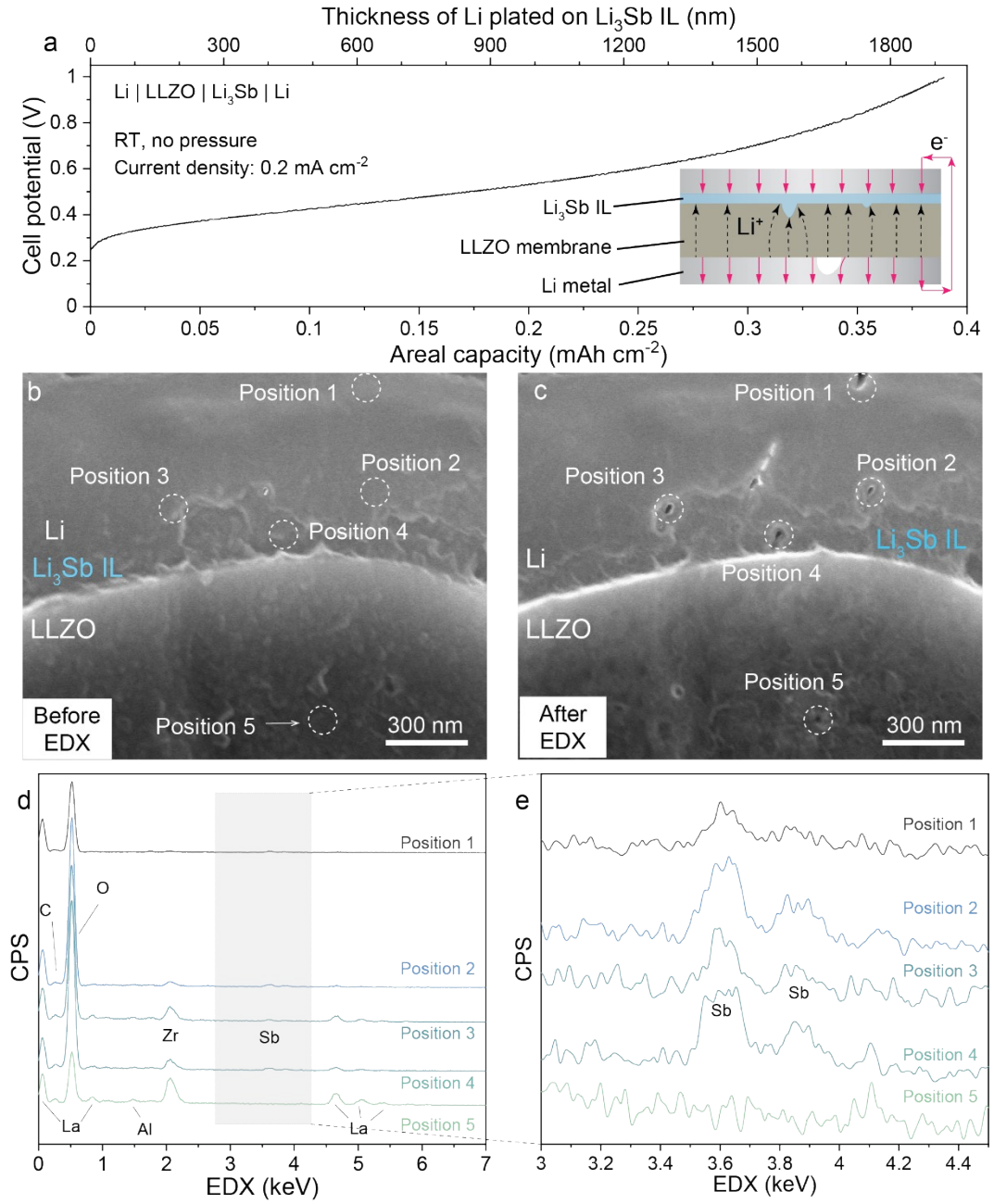

Fig. S20 Li plating experiments of Li | LLZO | Li_3Sb | Li by EDX-SEM. (a) Scheme and voltage profile of the Li | LLZO | Li_3Sb | Li symmetrical cell. The Sb coating was applied on one side of the LLZO membrane. Li was plated from the none-IL side to Li_3Sb IL. The voltage increasing indicates the void formation on the none-IL side. SEM images of the Li | Li_3Sb | LLZO cross-section (b) before and (c) after EDX measurements. (d-e) EDX spectra at different sampling positions.

Note S2 Li plating experiments of Li | LLZO | Li_3Sb | Li by EDX-SEM.

Given the high electronic conductivity of the Li_3Sb alloy, it is in principle possible that Li plating could occur at the Li_3Sb | LLZO interface, which might displace the interlayer from the SSE surface and compromise its function during subsequent stripping.

The stable overpotential observed in Li | Li_3Sb | LLZO | Li_3Sb | Li symmetric cells suggests that no new Li | LLZO interface is formed during cycling. To further examine the structural stability of the interlayer during Li plating, an experiment was designed to probe the spatial distribution of Sb across the Li/IL/LLZO interfaces.

A 10 nm thick Sb layer was magnetron sputtered onto one side of the LLZO membrane. Subsequently, two Li foils were isostatically pressed onto opposite sides of the LLZO membrane, forming an asymmetric Li | Li_3Sb | LLZO | Li cell, with Li | Li_3Sb as the working electrode and Li as the counter electrode, as schematically depicted in **Fig. S20a**. Next, a negative current density of (value) was applied over a (surface area) for 1 hour, leading to the deposition of *ca*. 2 μm of Li at the working electrode. The cell was then analyzed in depth using cross-sectional scanning electron microscopy (SEM) imaging combined with energy dispersive X-ray (EDX) analysis. As shown in the EDX data collected from selected points at the Li | Li_3Sb | LLZO interfacial region before and after Li plating (**Fig. S20**), Li deposition did not displace the Li_3Sb IL from the LLZO surface. In fact, even after plating a relatively large amount of Li (~2 μm thick), Sb remained clearly detectable (visually and qualitatively with SEM and EDX measurements) at the Li | LLZO interface, confirming the stability of the Li_3Sb interfacial layer during Li plating.

Notably, despite the high electronic conductivity of the Li_3Sb IL, the preferential Li plating at the Li | Li_3Sb interface rather than at the Li_3Sb IL | LLZO interface can be explained through surface energy considerations. Specifically, given the interfacial energy values of Li_3Sb | LLZO (-1.98 J m^{-2}), Li | Li_3Sb (-1.62 J m^{-2}), and Li | LLZO (-0.27 J m^{-2}),[3] one can conclude that Li plating at the Li_3Sb | LLZO interface is not thermodynamically favorable. This is because such plating would result in a more positive total Gibbs free energy compared to Li plating at the Li | Li_3Sb interface. In other words, Li deposition at the Li_3Sb | LLZO interface would lead to a decrease in the Li_3Sb | LLZO contact area while increasing the Li | Li_3Sb interface. Additionally, it would require the formation of a new Li | LLZO interface, which demands extra energy input, as indicated by the following equation: $\gamma_{Li/Li_3Sb} + \gamma_{Li/LLZO} - \gamma_{Li_3Sb/LLZO} = 0.09\ J\ m^{-2}$.

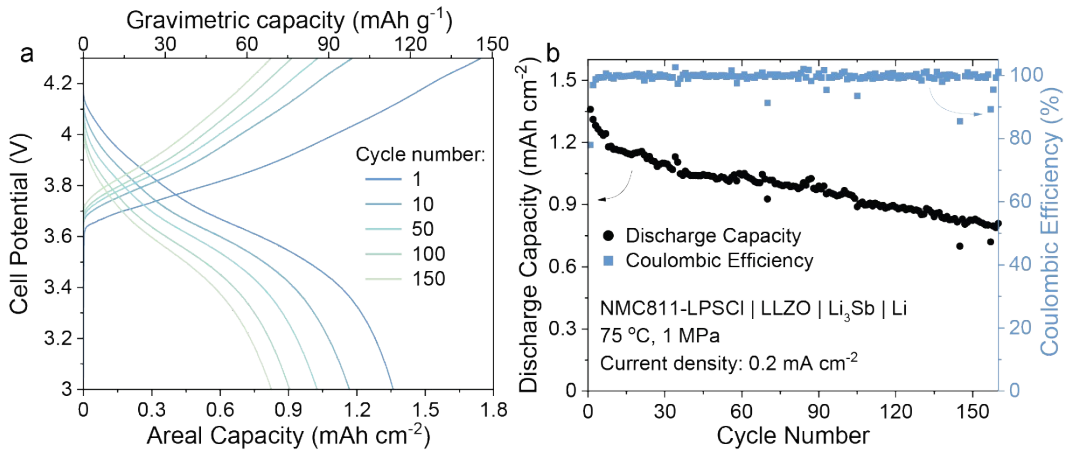

Fig. S21 Proof-of-concept all-solid-state batteries. Charge and discharge potential profiles (a) and capacity retention behavior (b) of NMC811-LPSCl | LLZO | Li_3Sb | Li ASSLB.

Note S3 Proof-of-concept all-solid-state batteries.

Following the assessment of the electrochemical performance of the Li metal anode in conjunction with LLZO membranes coated with a thick Li_3Sb IL using symmetric cell configurations, we extended our investigation to a full cell configuration, utilizing $LiNi_{0.8}Mn_{0.1}Co_{0.1}O_2$ (NMC811) as the cathode active material. The fabrication process of the all-solid-state full cell involved several steps. First, LLZO membranes were coated on one side (anode side) with 10 nm of Sb. As in the Li | LLZO-Sb | Li symmetric cells, Li foil was cold-isostatic-pressed (71 MPa for 3 minutes) onto the anode side of the membranes, followed by heating at 275 °C for 30 minutes to form the Li_3Sb IL. Meanwhile, a cathode tape was prepared by coating a carbon-coated aluminum foil with a composite mixture containing NMC811 as the active material, Li_6PS_5Cl (LPSCl) as the solid electrolyte, hydrogenated nitrile butadiene rubber (HNBR) as the binder, and vapor-grown carbon fiber (VGCF) as the conductive additive. The NMC811 loading was 12 mg cm^{-2}. The cathode tape was then attached to the LLZO surface of the as-prepared LLZO | Li_3Sb | Li membrane, followed by isostatic pressing at 160 MPa for 3 minutes. Notably, to mitigate degradation of the LPSCl solid-state electrolyte, $LiNbO_3$-coated (*ca*. 5 nm) NMC active material was used for the cathode fabrication, instead of pure NMC. VGCF was selected as the conductive additive due to its lower reactivity with LPSCl compared to other carbonaceous materials. HNBR was chosen as the binder to provide enhanced flexibility to the cathode tape.

To evaluate the performance of the prepared full cells, galvanostatic cycling was performed at a current density of 0.2 mA cm^{-2} between 3 and 4.3 V *vs*. Li^+/Li at 75 °C under uniaxial pressure of 1 MPa (**Fig. S21**). The initial charge and discharge capacities for the first cycle at 0.1 C were 146 mAh $gNMC^{-1}$ and 114 mAh $gNMC^{-1}$, respectively, resulting in an initial coulombic efficiency of 78%. The irreversible capacity loss during the first cycle is primarily attributed to the oxidation of LPSCl, a phenomenon extensively studied by Hu et al. [4] From the second cycle onward, the coulombic efficiency significantly improved, reaching over 99% for subsequent cycles. The cells exhibited capacity retention of 52% over 375 cycles. The degradation in capacity is likely due to the increasing overpotential of the cathode composites, resulting from

volume changes in NMC811 upon cycling and contact loss between NMC811 and LPSCl under relatively low stack pressure.[5, 6]

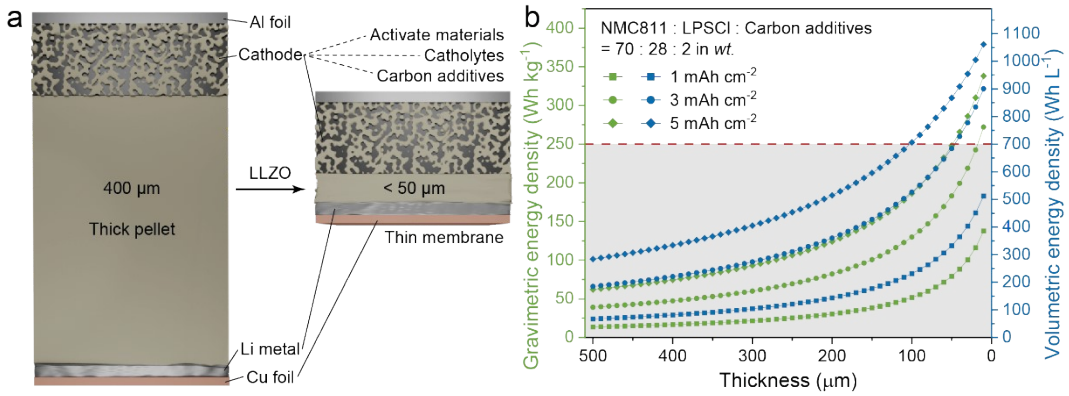

Fig. S22 Energy densities calculation based on LLZO SSEs. (a) Schematic representation of an all-solid-state battery (ASSB) employing a thick pellet and a thin membrane solid electrolyte separator. (b) Calculated gravimetric and volumetric energy density of NMC811-LPSCl | LLZO-Sb | Li ASSLBs, employing different cathode active material loading and different LLZO thicknesses.

Table S1 Diffusion coefficients of Li_3Sb.

The diffusion coefficient of Li_3Sb from DFT calculation and ionic conductivity of LLZO from Arrhenius equation in **Fig. S2** at different temperatures.

T	D_{Li3Sb}	σ_{Li3Sb}	σ_{LLZO}
°C	$cm^2\ s^{-1}$	$S\ cm^{-1}$	$S\ cm^{-1}$
25	1.48×10^{-7}	0.0465	4.22×10^{-4}
75	3.50×10^{-7}	0.0810	0.00216
125	6.66×10^{-7}	0.123	0.00718
175	1.10×10^{-6}	0.169	0.0180
225	1.64×10^{-6}	0.219	0.0372
275	2.27×10^{-6}	0.271	0.0667

Table S2 Parameters used in calculating energy density of NMC811-LPSCl | LLZO-Sb | Li full cells.

Parameters for Fig. S21		
Parameters	**Unit**	**Value**
Loading of NMC811	mg cm^{-2}	12
Thickness of cathode	μm	51.1
Ratio of NMC-Carbon-LPSCl	-	67.5:3.5:29 in weight
Gravimetric energy density	**Wh kg^{-1}**	**163**
Volumetric energy density	**Wh L^{-1}**	**611**

Parameters used for ASSBs in Fig. S22		
Parameters	**Unit**	**Value**
Thickness of Al current collector	μm	16
Density of NMC811	g cm^{-3}	4.77
Density of Carbon additives	g cm^{-3}	1.8
Density of LPSCl	g cm^{-3}	2.0
Ratio of NMC-Carbon-LPSCl	-	70:2:28 in weight
Theoretical capacity of NMC811	mAh g^{-1}	200
Average voltage	V	3.8
Density of LLZO	g cm^{-3}	5.1
Thickness of LLZO membrane	μm	45
Thickness of Li anode	μm	10
Thickness of Cu current collector	μm	12

Supplementary References

1. A. Jain, S. P. Ong, G. Hautier, W. Chen, W. D. Richards, S. Dacek, S. Cholia, D. Gunter, D. Skinner, G. Ceder and K. A. Persson, *Apl. Mater.*, 2013, **1**.
2. M. K. Horton, P. Huck, R. X. Yang, J. M. Munro, S. Dwaraknath, A. M. Ganose, R. S. Kingsbury, M. J. Wen, J. X. Shen, T. S. Mathis, A. D. Kaplan, K. Berket, J. Riebesell, J. George, A. S. Rosen, E. W. C. Spotte-Smith, M. J. McDermott, O. A. Cohen, A. Dunn, M. C. Kuner, G. M. Rignanese, G. Petretto, D. Waroquiers, S. M. Griffin, J. B. Neaton, D. C. Chrzan, M. Asta, G. Hautier, S. Cholia, G. Ceder, S. P. Ong, A. Jain and K. A. Persson, *Nat. Mater.*, 2025, **24**, 1522-1532.
3. G. Q. Zhao, C. W. Luo, B. Wu, M. Y. Zhang, H. Q. Wang and Q. S. Hua, *ACS Appl. Mater. Inter.*, 2023, **15**, 50508-50521.
4. X. Hu, Z. Zhao, Y. Zhao, X. Wang, S. Sainio, D. Nordlund, C. M. Ruse, X.-D. Zhou, S. W. Boettcher, D. Hou, Q.-J. Hong and L. Mu, *J. Mater. Chem. A*, 2024, **12**, 3700-3710.
5. F. Y. Zhang, Y. N. Guo, L. Q. Zhang, P. Jia, X. Liu, P. Qiu, H. B. Zhang and J. Y. Huang, *Etransportation*, 2023, **15**.
6. C. Doerrer, I. Capone, S. Narayanan, J. L. Liu, C. R. M. Grovenor, M. Pasta and P. S. Grant, *ACS Appl. Mater. Inter.*, 2021, **13**, 37809-37815.